EES Catalysis

PAPER

View Article Online
View Journal



Cite this: DOI: 10.1039/d6ey00024j

# Interdigitated MgO/Au front selective contacts for enhanced photocatalytic systems based on $TiO_2$ as light-absorber

Oriol Segura-Blanch, *[ab] Eloi Ros,[c] Asier Agrelo-Lestón,[bde] Edoardo Maggi,[abd] Lorenzo Calvo-Barrio,[fg] Jordi Llorca,[bd] Lluís Soler,[bd] Marcel Placidi,[abh] Cristóbal Voz,[ab] Edgardo Saucedo[ab] and Joaquim Puigdollers[ab]

Received 31st January 2026,
Accepted 12th April 2026

DOI: 10.1039/d6ey00024j

rsc.li/eescatalysis

Selective charge extraction is a central limitation in heterogeneous photocatalysis, where short carrier diffusion lengths and interfacial recombination strongly restrict efficiency. Here we translate the photovoltaic concept of selective contacts to photocatalytic systems by designing interdigitated front architectures on a planar $TiO_2$ absorber. Magnesium–magnesium oxide (Mg–$MgO_x$) is used as an electron-selective layer, while gold nanoparticles act simultaneously as hole-selective contacts, plasmonic enhancers, and charge-transfer mediators toward gas-phase reactants. Interdigitated Mg–$MgO_x$/Au patterns with controlled coverage and perimeter were fabricated on sol–gel anatase $TiO_2$ films and tested for hydrogen production from ethanol–water vapor mixtures under UV illumination. While Au nanoparticles alone strongly enhance activity through efficient hole extraction and plasmonic effects, the addition of Mg–$MgO_x$ enables selective electron collection. However, performance is not governed by Mg–$MgO_x$ coverage alone. Samples with similar Mg–$MgO_x$ area fractions but different geometries show markedly different hydrogen production rates. To rationalize this behavior, we introduce a dimensionless geometric parameter $\eta$, defined as the normalized ratio between selective-contact perimeter and coverage. Hydrogen production follows a Langmuir–Hinshelwood-type kinetic model when expressed as a function of $\eta$, demonstrating that interfacial length, rather than area alone, controls the number of photogenerated carriers that reach adsorbed reactants before recombining. Highly interdigitated samples show up to a twofold increase in hydrogen production compared to non-patterned $TiO_2$/Au references, despite having comparable material composition.

## Broader context

Sustainable hydrogen production is a cornerstone of global efforts to decarbonize energy systems, enabling low-carbon fuel cycles and providing storage pathways for intermittent renewable electricity. Photocatalysis, the direct use of sunlight to drive chemical reactions, offers a scalable route to produce hydrogen without electricity or high-temperature processes, but its efficiency is fundamentally limited by rapid recombination of photogenerated charge carriers at interfaces. In this work, we adapt selective contact concepts from photovoltaic technology to photocatalytic systems by engineering interdigitated electron- and hole-selective regions on a planar titanium dioxide ($TiO_2$) absorber. Specifically, magnesium–magnesium oxide (Mg–$MgO_x$) acts as an electron extractor while gold nanoparticles serve both as hole collectors and plasmonic enhancers. Through systematic experimentation with varying contact geometries, we show that hydrogen production is governed not by material coverage alone but by the interplay between interface length and carrier extraction efficiency, captured by a new dimensionless geometric parameter. Our findings reveal that optimized interdigitated architectures can nearly double hydrogen yield compared with non-patterned references. These insights provide a generalizable design principle for enhancing photocatalytic performance and help bridge the gap between fundamental photocatalysis research and the development of practical solar-to-fuel technologies.

[a] Universitat Politècnica de Catalunya (UPC), Photovoltaic Lab - Micro and Nano Technologies Group (MNT), Electronic Engineering Department, EEBE, Av Eduard Maristany 10-14, Barcelona 08019, Catalonia, Spain. E-mail: oriol.segura.blanch@upc.edu
[b] Universitat Politècnica de Catalunya (UPC), Barcelona Center in Multiscale Science and Engineering, EEBE, Av Eduard Maristany 10-14, Barcelona 08019, Catalonia, Spain
[c] Departament de Química Inorgànica, Universitat de Barcelona, Diagonal 645, E-08028, Barcelona, Spain
[d] Institute of Energy Technologies and Department of Chemical Engineering, Universitat Politècnica de Catalunya (UPC), Eduard Maristany 16, EEBE, Barcelona 08019, Spain
[e] Center for Cooperative Research on Alternative Energies (CIC energiGUNE), Basque Research and Technology Alliance (BRTA), Alava Technology Park, Albert Einstein 48, Vitoria-Gasteiz 01510, Spain
[f] Centres Científics i Tecnològics(CCiTUB), Universitat de Barcelona, Carrer de Lluís Solé i Sabarís 1, 08028 Barcelona, Spain
[g] IN2UB, Departament d'Enginyeria Electrònica i Biomèdica, Universitat de Barcelona, Carrer de Martí i Franquès 1, 08028 Barcelona, Spain
[h] Institut de Recerca en Energia de Catalunya (IREC), Jardins de les Dones de Negre 1, Sant Adrià del Besòs 08930, Catalonia, Spain

# 1. Introduction

Photocatalysis enables the direct conversion of solar energy into chemical fuels by coupling light absorption with surface redox reactions. Among the processes explored, water splitting and the photo-reforming of simple hydrocarbons have attracted particular attention as routes for hydrogen production.[1] Hydrogen is a clean and energy-dense fuel that can act as both an energy carrier and storage medium, highlighting photocatalysis as a promising approach for solar-to-fuel technologies.[2]

Photocatalytic performance is fundamentally limited by non-radiative recombination, largely arising from defect-induced mid-gap states in the semiconductor. A common strategy to mitigate these losses is to increase crystallinity while reducing characteristic dimensions, thereby shortening the distance that photogenerated carriers must travel to reach the surface. When this transport length approaches the carrier diffusion length, recombination losses are reduced and photocatalytic efficiency improves.

Beyond bulk recombination, photocatalytic performance is also limited by inefficient carrier transport and extraction to active reaction sites. This is typically addressed by incorporating co-catalysts, which enhance carrier extraction and facilitate charge transfer from the solid to the surrounding medium. Metallic nanoparticles, particularly noble metals, are widely used due to their multifunctional role: they can promote interfacial charge transfer, induce band bending through their high work function, and, in some cases, enhance light absorption *via* localized surface plasmon resonance.[3]

An alternative approach to improve charge separation involves engineering semiconductor heterojunctions, such as Z-scheme and S-scheme configurations.[4] These architectures exploit favorable band alignments to spatially separate electrons and holes, thereby reducing recombination. In addition, combining semiconductors with different band gaps can extend light absorption across a broader spectral range.[5]

In solar cell technology, charge separation and extraction are achieved using transport materials and selective contacts, commonly referred to as electron and hole transport layers (ETLs and HTLs). These layers selectively extract one type of carrier while blocking the other, thereby reducing interfacial recombination and enforcing spatial separation of electrons and holes. In addition, they often provide surface passivation, further suppressing recombination at the absorber interface. This combined effect has been central to the efficiency improvements achieved in modern photovoltaic devices.[6]

From this perspective, the widespread use of metallic co-catalysts and semiconductor heterojunctions in photocatalysis can be viewed as conceptually analogous to selective contacts in solar cells.[3] More broadly, selective contacts describe interfacial layers that promote directional carrier extraction, enforce spatial separation of electrons and holes, and suppress recombination losses.[7,8] While these principles have been systematically exploited in photovoltaics to achieve record efficiencies at both laboratory[9,10] and commercial scales,[11] their implementation in photocatalysis remains less controlled at the device level.

Applying the selective-contact paradigm to photocatalysis is not straightforward. Most photocatalysts exhibit highly nanostructured morphologies, which makes the controlled integration of separate electron- and hole-transport layers difficult. Although a few studies have demonstrated such architectures,[12–14] their fabrication remains complex and has not yet become a broadly applicable strategy.

In this work, we extend the selective-contact concept to a photocatalytic device based on a planar $TiO_2$ absorber. Gold nanoparticles (Au NPs) are incorporated as multifunctional elements that act both as hole-selective contacts and as charge-transfer mediators between the solid-state device and gas-phase reactants. In addition, a Mg–$MgO_x$ electron-transport layer is introduced to enhance charge separation and extraction. Within this architecture, the $TiO_2$/Au interface preferentially extracts photogenerated holes to drive alcohol oxidation, while the $TiO_2$/Mg–$MgO_x$ interface selectively collects electrons. Au nanoparticles deposited on the Mg–$MgO_x$ regions further facilitate electron transfer toward hydrogen evolution reaction (Fig. 1a).

To spatially organize these selective extraction pathways, we adopt the photovoltaic concept of interdigitated contacts. In solar cells, interdigitated architectures eliminate front-side metallization shading by relocating metallic contacts to the rear of the device. Their design is governed by the carrier diffusion lengths in the absorber, allocating larger collection areas to minority carriers while majority carriers can be collected over wider regions due to their longer diffusion lengths.[15,16] In the present photocatalytic system, interdigitated contacts are likewise advantageous because oxide semiconductors typically exhibit short carrier diffusion lengths. Moreover, under continuous gas-flow operation the lifetime of reactive intermediates is limited, requiring oxidation and reduction sites to be placed in close proximity to suppress back reactions caused by local charge imbalance (Fig. 1b).

Using this approach, we fabricate and characterize photocatalytic devices with interdigitated Mg–$MgO_x$/Au selective contacts and evaluate their hydrogen production performance. Unlike previously reported strategies based on nanoscale separated dual cocatalyst decoration[12–14,17] or facet-dependent redox separation,[18–20] the interdigitated architecture is implemented at the device scale (hundreds of micrometers to millimeters), enabling controlled spatial organization of electron- and hole-extraction pathways across the absorber surface. Although a semiconductor junction is present, this architecture differs fundamentally from Z-scheme or S-scheme photocatalysts because the $MgO_x$ layer is ultrathin and does not contribute to light absorption, acting instead purely as an electron-selective contact. By correlating photocatalytic activity with both the device electronic structure and the geometry of the interdigitated pattern, we demonstrate that device-level contact architecture can strongly influence photocatalytic performance.

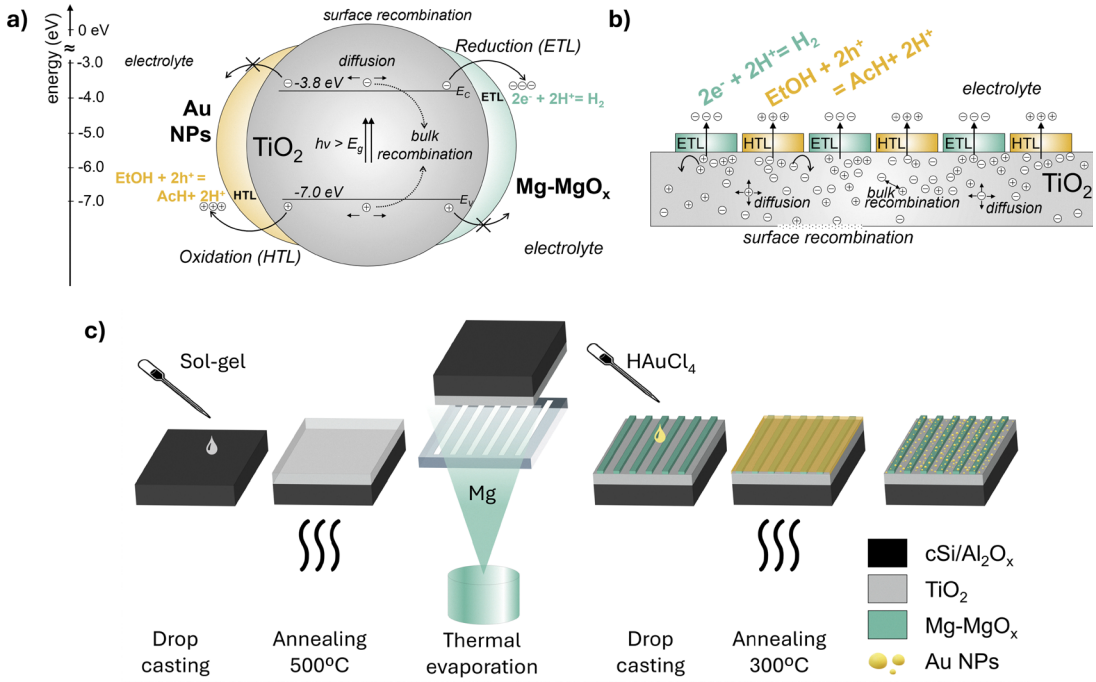


Fig. 1 (a) Energy-level schematic of the photocatalytic process in a generic nanostructured $TiO_2$ absorber incorporating ETL and HTL layers. (b) Schematic illustration of the electronic and photocatalytic processes occurring in a planar $TiO_2$ device equipped with ETL and HTL contacts. (c) Fabrication steps of the interdigitated samples investigated in this work.

## 2. Experimental section

### 2.1. Preparation of $TiO_2$ thin films

$TiO_2$ thin films were prepared by a sol–gel method using titanium(IV) propoxide as precursor. The precursor was dissolved in absolute ethanol under an argon atmosphere and hydrolyzed by the controlled addition of hydrochloric acid and water under continuous stirring. The resulting sol was diluted with ethanol to obtain a deposition solution.

Silicon wafers coated with an insulating $Al_2O_x$ layer deposited by atomic layer deposition ($cSi/Al_2O_x$) were used as substrates. The substrates were cut into 2 × 2 $cm^2$ pieces and coated by drop casting the $TiO_2$ sol, followed by drying at room temperature for 24 h. The films were calcined in air at 500 °C for 4 h (5 °C $min^{-1}$ ramp) to obtain anatase $TiO_2$. To minimize cracking and ensure full surface coverage, three successive $TiO_2$ layers were deposited. The resulting $TiO_2$ absorber films had a typical thickness of 1.5 ± 0.3 μm.

### 2.2. Fabrication of interdigitated front contacts

Magnesium electron-selective contacts were deposited by thermal evaporation in a glovebox-integrated UNIVEX 350G vacuum system at a base pressure of $\sim 10^{-5}$ mbar. Deposition was monitored using a quartz crystal microbalance, yielding Mg layers with a nominal thickness of 10 nm. Interdigitated patterns were defined using manually assembled shadow masks made from simple mechanical spacers and masking materials. After deposition, samples were stored under nitrogen atmosphere to limit uncontrolled Mg oxidation.

Gold nanoparticles were introduced by drop casting 150 μL of a 0.1125 M $HAuCl_4$ solution, corresponding to a 1 : 100 Au : $TiO_2$ mass ratio. The samples were dried at 50 °C and annealed at 300 °C for 1 h in air to form and anchor Au nanoparticles on the $TiO_2$ surface.

### 2.3. Photocatalytic hydrogen production

Photocatalytic experiments were carried out in a continuous-flow glass reactor using a gaseous ethanol–water mixture (9 : 1 molar ratio) carried by argon (20 mL $min^{-1}$). Samples were illuminated using a 500 W Hg–Xe solar simulator delivering UV-A irradiance of 72 mW $cm^{-2}$ at the sample surface. Reaction products were monitored online by micro–gas chromatography.

Further experimental details, including the detailed fabrication procedures, characterization methods and photocatalytic measurement protocols, are provided in the SI.

## 3. Results and discussions

### 3.1. Sample characterization

We fabricated several samples with different Mg layer geometries. Table S1 shows 3D sketches of the most representative samples together with the geometric characteristics of the Mg interdigitated patterns. Samples are labeled as T–Mg*X*–Au, where T denotes the $TiO_2$ catalytic absorber and the increasing values of *X* correspond to a more interdigitated pattern of Mg that results in a larger perimeter of the Mg–$MgO_x$ pattern.

The $TiO_2$ absorber layer was first examined by Raman spectroscopy. The spectra confirmed the presence of the anatase phase[21] with no detectable traces of rutile or brookite, the other two common $TiO_2$ polymorphs (Fig. S2). The surface morphology of the absorber was investigated by SEM, revealing a continuous $TiO_2$ layer containing cracks; however, these cracks did not reach the underlying c-Si/$Al_2O_x$ substrate due to the deposition of three consecutive sol–gel layers (Fig. S3a and b). Owing to the ultrathin nature of the Mg films, Mg deposited onto $TiO_2$ can infiltrate these cracks, but it does not fill them or coat them conformally (Fig. S3c and d).

XPS analysis of the Ti 2p and O 1s core levels further verified the presence of $TiO_2$ films for samples containing both Mg and Au (Fig. 2a, b and Fig. S4a, b). The Mg 1s peak at 1304.6 eV[22] (Fig. 2c) and the Mg 2p peak at 51.0 eV[23] (Fig. 2d) confirm that the Mg layer was fully oxidized to $MgO_x$ during the annealing step required for Au nanoparticle formation. This is expected due to the air atmosphere used during the heat treatment. Importantly, this oxidation is beneficial for the device design: transforming metallic Mg into $MgO_x$ converts the $TiO_2$/Mg interface from a Schottky junction into a semiconductor/ETL junction, since $MgO_x$ is a well-known ETL in various photovoltaic absorbers.[24–26] Complementary STEM and HR-EDX analysis of the T–Mg1–Au sample further support this interpretation. The oxygen signal extends over the Ti signal in regions where Mg is present, matching the spatial distribution of Mg and providing an additional confirmation of Mg oxidation (Fig. 2g). The maps also show that although the Mg–$MgO_x$ layer and the Au nanoparticles percolate through the surface cracks of the $TiO_2$, there is no significant signal from either species deeper inside the film, indicating that the cracks do not fully penetrate the $TiO_2$ layer.

Analysis of the Au 4f core levels in the T–Au sample (Fig. 2f) shows fully metallic gold, with the Au $4f_{7/2}$ and $4f_{5/2}$ peaks located at 84.0 eV and 87.7 eV,[27,28] respectively. The T–Mg1–Au sample also exhibits these metallic Au peaks; however, additional $Au^{\delta+}$ components appear (Fig. 2e), with Au $4f_{7/2}$ and $4f_{5/2}$ peaks at 85.2 eV and 89.0 eV, which correspond to oxidized gold species. Such energy shifts and oxidation states are typical for Au–O–Mg interfacial environments, indicating the formation of Au–O–Mg linkages. This interfacial chemistry provides a likely explanation for the stronger adhesion of Au and the enhanced dispersion of Au nanoparticles on the Mg–$MgO_x$ surface compared with bare $TiO_2$.[29]

Fig. 3a shows that the mean Au NPs diameter on $TiO_2$ is approximately 30 nm, whereas NPs grown on Mg–$MgO_x$ exhibit a larger average diameter of over 40 nm. The presence of oxidized Au species at the interface may contribute to this different growth behavior. In both cases, smaller nanoparticles are also present and appear to percolate into $TiO_2$ cracks and surface roughness; however, their precise size is difficult to determine from SEM images alone. For a more interdigitated

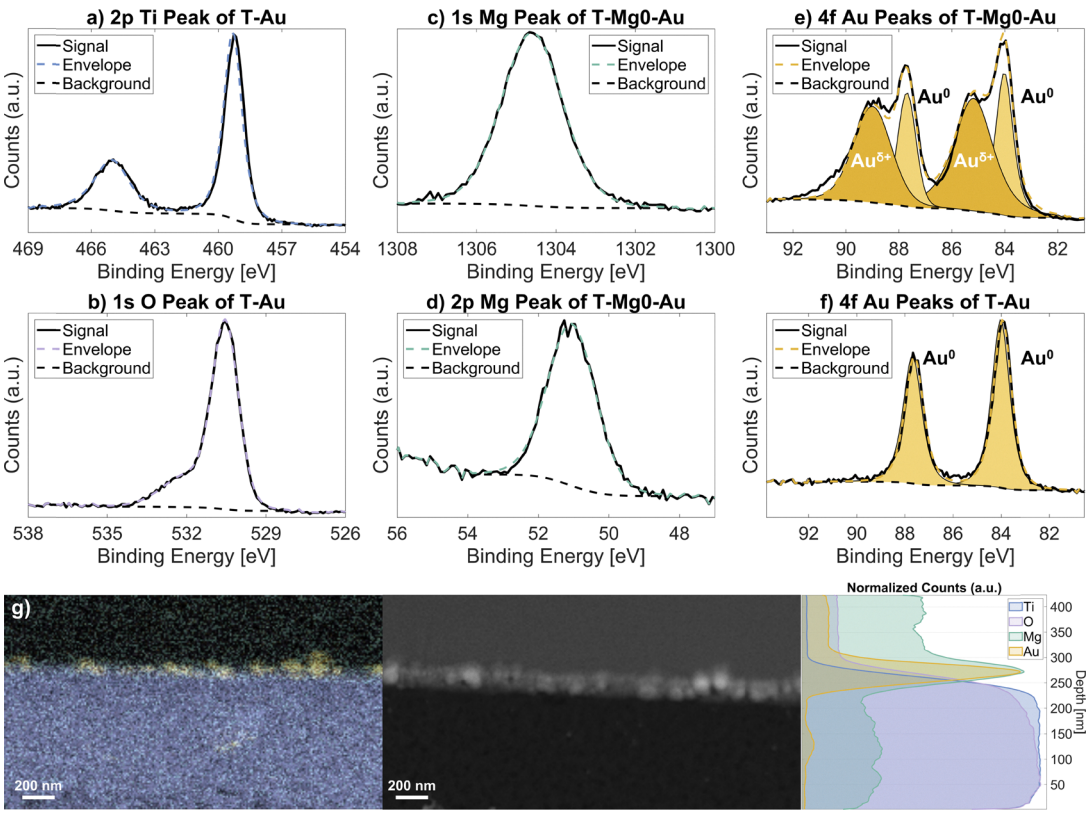


Fig. 2 (a) Ti 2p XPS peak of the T–Au ($TiO_2$/Au) sample. (b) O 1s XPS peak of the T–Au sample. (c) Mg 1s XPS peak of the T–Mg1–Au sample. (d) Mg 2p XPS peak of the T–Mg1–Au sample. (e) Au 4f XPS peaks of the T–Mg1–Au ($TiO_2$/Mg–$MgO_x$(full coverage)/Au) sample. (f) Au 4f XPS peaks of the T–Au sample. (g) HR-EDXS map, STEM image and elemental line profile of the cross-section of the T–Mg1–Au sample.

sample, such as T–Mg4–Au, SEM-EDX mapping confirms that the Au distribution follows the Mg interdigitated geometry, with a clearly higher Au signal on the Mg–$MgO_x$ regions than on the bare $TiO_2$ areas (Fig. 3c). These results collectively support the strong interaction between Au and the Mg–$MgO_x$ layer, consistent with previous reports of Au–O–Mg bonding influencing nanoparticle size, adhesion, and dispersion.

### 3.2. Hydrogen production

The photocatalytic activity of the samples was evaluated, and the results are summarized in Table 1, Fig. S5, S6 and Table S2. The bare $TiO_2$ sample produces a measurable amount of hydrogen; however, the quantity of acetaldehyde detected is more than six times higher than the generated $H_2$. This indicates that a significant fraction of the produced hydrogen recombines with residual oxygen in the chamber before reaching the gas chromatograph.

Introducing Au nanoparticles dramatically enhances the photocatalytic response: the T–Au sample produces more than twenty times the hydrogen generated by bare $TiO_2$. This improvement arises from several synergistic effects. First, due to the much higher work function of gold ($\Phi_{Au} \approx 5.3$ eV[30]) compared with $TiO_2$ ($\Phi_{TiO_2} \approx 4.4$ eV[31]), Fermi level equilibration induces charge redistribution at the $TiO_2$/Au interface. This creates a depletion region in $TiO_2$ and an upward band bending that suppresses electron transfer from $TiO_2$ to Au while promoting hole extraction into the metal, effectively forming a HTL.[32] Incorporating an HTL is especially beneficial because the fabricated anatase is typically highly n-doped,[33] and minority carrier (hole) collection is otherwise inefficient.

Second, the nanometric Au particles exhibit localized surface plasmon resonance (LSPR), enabling strong visible-light absorption. Plasmonic excitation generates hot carriers and increases the local temperature. Hot electrons can be injected into $TiO_2$ and subsequently participate in the photocatalytic reaction, thereby extending photoresponse into the visible range,[34] whereas pristine anatase absorbs only in the UV. The modest temperature rise induced by LSPR also accelerates surface reaction kinetics *via* the Arrhenius relation. Although higher temperatures can increase charge recombination in $TiO_2$, the operating temperature of the samples remained below ~75 °C, ensuring that the enhancement in reaction kinetics outweighed any recombination losses.[35]

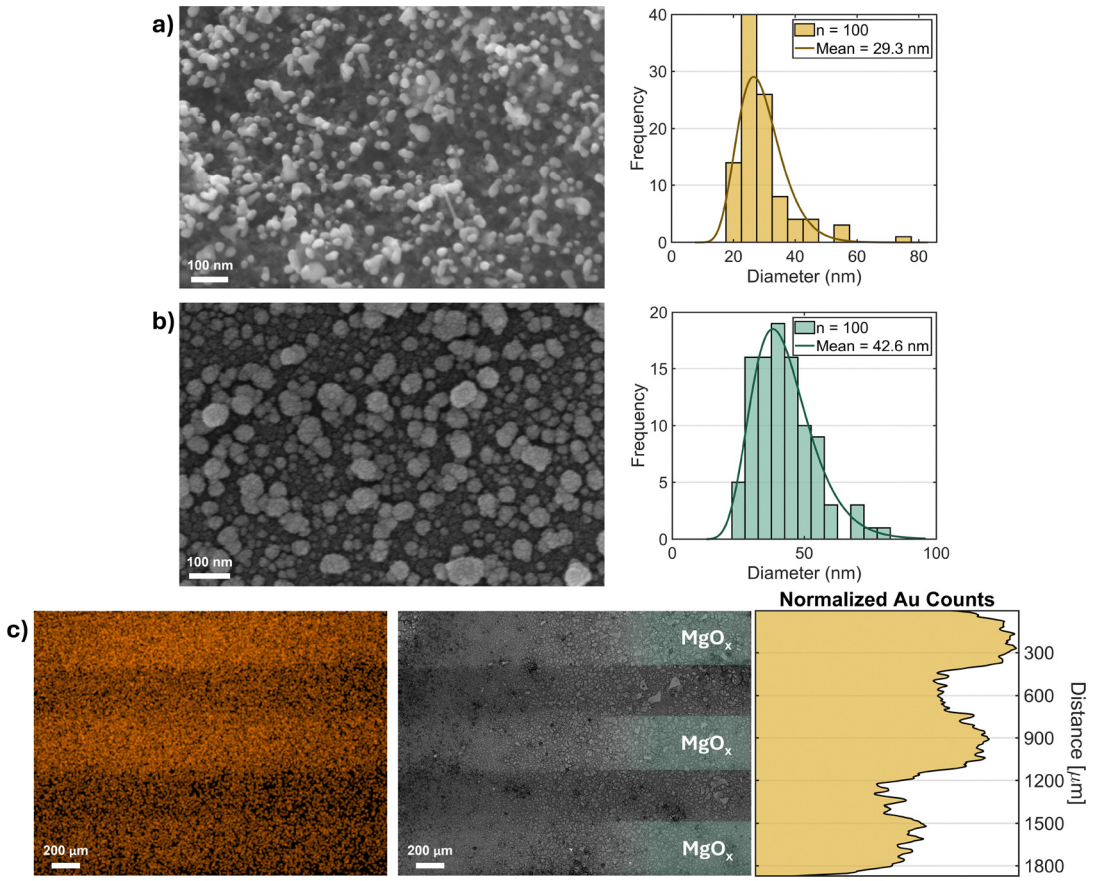


Fig. 3 (a) SEM image of the surface of the T–Au ($TiO_2$/Au) sample and the diameter distribution of the observed Au NPs. (b) SEM image of the surface of the T–Mg1–Au ($TiO_2$/Mg–$MgO_x$(full coverage)/Au) sample and the corresponding diameter distribution of the Au NPs. The Au NPs outlines correspond to fitted log-normal distributions. (c) EDX Au map, SEM image and Au line profile of the surface of the T–Mg4–Au ($TiO_2$/Mg–$MgO_x$(highly interdigitated)/Au) sample.

Table 1 Table summarizing the geometric parameters of the ETL patterns for all samples (eqn (8)), the amount of hydrogen produced during the first two hours, the mean $H_2$ production rate over that period, and the corresponding peak $H_2$ generation rate

| Sample | Mg coverage [%] | Mg perimeter [mm] | Geometric factor [$\eta$] | $H_2$ generated during 2 h [mmol $g^{-1}$] | Mean $H_2$ generation rate [μmol $min^{-1}$ $g^{-1}$] | Maximum $H_2$ generation rate [μmol $min^{-1}$ $g^{-1}$] |
|---|---|---|---|---|---|---|
| Bare $TiO_2$ | — | — | — | 0.3 | 2.9 | 3.6 |
| T–Au | — | — | — | 8.0 | 66.2 | 86.4 |
| T–Mg1 | ∼100 | ∼8 | ∼0.1 | 0.03 | 0.2 | 0.7 |
| T–Mg2 | ∼50 | ∼28.3 | ∼0.7 | 0.03 | 0.2 | 0.7 |
| T–Mg1–Au | 98.6 | 8.6 | 0.1 | 4.8 | 40.0 | 57.9 |
| T–Mg2–Au | 50.7 | 27.6 | 0.7 | 10.7 | 88.7 | 109.3 |
| T–Mg3–Au | 24.3 | 198.2 | 10.7 | 15.7 | 130.0 | 170.5 |
| T–Mg4–Au | 53.2 | 991.4 | 22.8 | 16.0 | 133.8 | 166.9 |

To further substantiate this enhancement in performance, the hydrogen production results were correlated with time-resolved photoluminescence (TRPL) measurements (Fig. 4a and Table 2). The decay curves were fitted using a biexponential model (eqn (S1)), from which the average lifetime[36] was calculated (eqn (S2)). For the $TiO_2$/Au sample, the fast decay component ($\tau_1$) is shorter than that of bare $TiO_2$, while the slow decay component ($\tau_2$) is slightly prolonged. These effects are reflected in the average lifetime ($\tau_{avg}$), which is lower for $TiO_2$/Au despite its significantly higher hydrogen production. This apparent contradiction can be rationalized by considering the photoluminescence quenching induced by Au nanoparticles, as reported in similar $TiO_2$-based systems.[37,38]Therefore, although the $TiO_2$/Au sample exhibits shorter lifetimes, this behavior is consistent with improved charge separation and enhanced photocatalytic activity.

When Mg–$MgO_x$ is deposited without Au, either across the full surface (T–Mg1) or in partially covered geometries (T–Mg2), the photocatalytic activity decreases sharply, with hydrogen production falling to roughly one tenth of that of bare $TiO_2$. This behavior reflects the electronic roles of the materials: although $MgO_x$ is an effective electron-selective layer, the anatase $TiO_2$ used here is strongly n-type, meaning that hole extraction, not electron extraction, is the limiting step. Extensive $MgO_x$ coverage therefore prioritizes majority-carrier extraction at the expense of minority-carrier collection, reducing overall reaction rates. In the extreme case of full Mg coverage, only cracks and small uncovered regions remain available for hole extraction, explaining the substantial drop in catalytic activity.

The TRPL results support this interpretation. The T–Mg1 sample exhibits the longest lifetimes ($\tau_1$, $\tau_2$, and $\tau_{avg}$), indicating reduced recombination and confirming that Mg–$MgO_x$ effectively improves charge separation. However, this improvement does not translate into higher hydrogen production, demonstrating that efficient carrier separation alone is insufficient to drive the reaction in the absence of effective surface charge transfer pathways.

Upon incorporation of Au nanoparticles (T–Mg1–Au and T–Mg2–Au), the hydrogen production increases markedly, while the measured lifetimes decrease relative to T–Mg1 but remain higher than those of the $TiO_2$/Au reference in terms of $\tau_1$ and $\tau_{avg}$. This combination of trends indicates that Mg–$MgO_x$ enhances charge separation, whereas Au nanoparticles are essential to enable efficient surface reactions. In addition to acting as a hole-selective contact and promoting plasmonic carrier generation, Au nanoparticles deposited on Mg–$MgO_x$ facilitate charge transfer by lowering overpotential barriers at solid–gas and solid–electrolyte interfaces,[39] thereby improving overall catalytic efficiency.

With both ETL ($MgO_x$) and HTL (Au) present, the system recovers performance. However, in T–Mg1–Au, the area devoted to electron extraction remains too large relative to the region available for hole transfer, limiting the improvement. Reducing the $MgO_x$ coverage, as in T–Mg2–Au, leads to a more balanced configuration between electron and hole extraction, allowing this sample to outperform even the T–Au reference.

The next step was to explore more intricate designs to evaluate how the trade-off between the active area devoted to electron and hole extraction evolves with geometry. For this purpose, the T–Mg3–Au and T–Mg4–Au samples were fabricated and tested. Both architectures produce approximately twice the hydrogen generated by the T–Au reference. Although T–Mg3–Au exhibits the highest peak production rate, the total hydrogen yield and average production over the first two hours are higher for T–Mg4–Au.

A comparison of their geometrical parameters reveals that T–Mg3–Au has the lowest Mg–$MgO_x$ coverage (∼24%), whereas T–Mg4–Au approaches ∼50%, similar to T–Mg2–Au, which nevertheless produces ∼40% less hydrogen. This indicates that surface coverage alone does not govern performance. Instead, the dominant difference lies in the perimeter of the Mg–$MgO_x$ patterns: T–Mg4–Au exhibits a perimeter approximately five times larger than that of T–Mg3–Au, while T–Mg3–Au itself has more than seven times the perimeter of T–Mg2–Au. These observations highlight the critical role of interface density, suggesting a strong interplay between active area, perimeter, and carrier extraction efficiency.

TRPL measurements further support this interpretation. The most interdigitated sample, T–Mg4–Au, exhibits slightly longer lifetimes ($\tau_1$, $\tau_2$, and $\tau_{avg}$) compared to T–Mg1–Au and T–Mg2–Au, although all values remain within the same range. This relatively modest variation indicates that bulk recombination dynamics are not significantly altered by increasing interdigitation. Instead, the performance enhancement arises from improved spatial organization of charge extraction and reaction

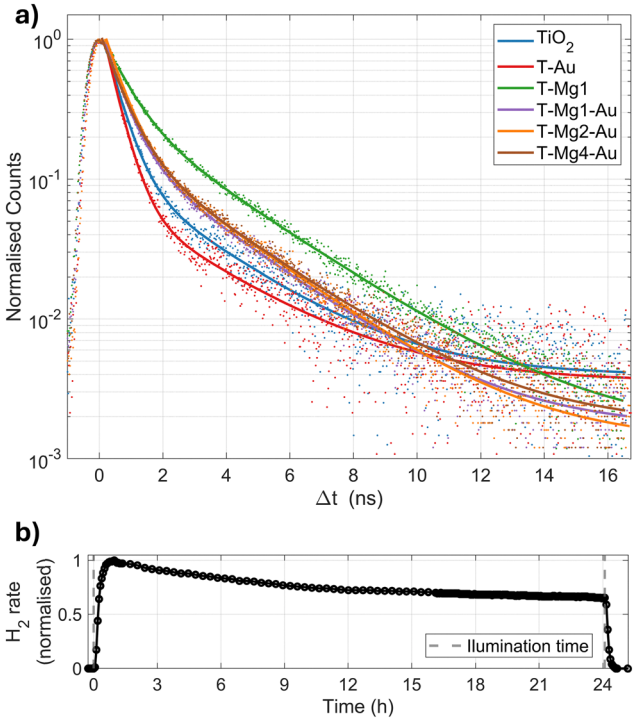


Fig. 4 (a) Time-resolved photoluminescence (TRPL) decay curves of representative samples, highlighting variations in charge carrier dynamics across different contact architectures. (b) Normalized hydrogen production rate as a function of time for the T–Mg4–Au sample during extended photocatalytic operation. The sample was remeasured several months after the initial 2 h photocatalytic test. The production rate is normalized to the peak value of each cycle to highlight the relative activity decay and stability over time.

Table 2 Bi-exponential fitting (eqn (S1)) parameters extracted from TRPL decay curves for the different samples. The table reports the reduced chi-squared ($\chi^2$), fast and slow decay components ($\tau_1$ and $\tau_2$), intensity-weighted average lifetime ($\tau_{avg}$ from eqn (S2)), amplitudes ($B_1$ and $B_2$), and background offset ($A$) obtained from the fits of curves in Fig. 4

| Sample | $\chi^2$ | $\tau_1$ (ns) | $\tau_2$ (ns) | $\tau_{avg}$ (ns) | $B_1$ | $B_2$ | $A$ |
|---|---|---|---|---|---|---|---|
| $TiO_2$ | 1.022 | 0.46 | 2.65 | 1.47 | 3391.8 | 512.5 | 243.8 |
| T–Au | 1.104 | 0.42 | 2.86 | 1.28 | 4046.7 | 325.3 | 251.9 |
| T–Mg1 | 1.160 | 0.70 | 2.87 | 2.31 | 1864.6 | 1309.0 | 26.0 |
| T–Mg1–Au | 1.103 | 0.55 | 2.64 | 1.63 | 3972.1 | 871.8 | 60.3 |
| T–Mg2–Au | 1.096 | 0.54 | 2.65 | 1.64 | 4234.8 | 931.5 | 46.7 |
| T–Mg4–Au | 1.010 | 0.59 | 2.76 | 1.68 | 4287.4 | 919.2 | 54.7 |

sites. The interdigitated geometry enables electrons and holes to be extracted at distinct but closely spaced regions, facilitating efficient charge separation while maintaining short diffusion paths for surface intermediates involved in ethanol dehydrogenation. As a result, the benefits of interdigitation extend beyond what is captured by TRPL, which primarily probes bulk recombination, and include improved coupling between charge extraction and surface reaction kinetics.

Moreover, the photocatalytic stability of the best-performing sample (T–Mg4–Au) was evaluated after several months of storage under ambient conditions in the dark, followed by extended operation (Fig. 4b). The peak hydrogen production at the beginning of this new measurement (113.3 μmol $min^{-1}$ $g^{-1}$) closely matches the final value recorded at the end of the initial 2 h cycle (116.5 μmol $min^{-1}$ $g^{-1}$), indicating good preservation of the catalytic activity over time. During 24 h of continuous operation, the activity gradually decreases to approximately 65% of the peak value within that cycle (74.0 μmol $min^{-1}$ $g^{-1}$). After this extended test, the sample was allowed to rest, exposed to air, and subsequently remeasured (full second and third cycles shown in Fig. S7). In the following 14.5 h cycle, the peak production reached 81.2 μmol $min^{-1}$ $g^{-1}$, with the activity stabilizing at around 70% of this peak value (57.0 μmol $min^{-1}$ $g^{-1}$). Although the hydrogen production rate does not remain strictly constant over time, the system exhibits a relatively stable and resilient behavior under operating conditions, with partial recovery upon air exposure. This behavior suggests that the mild deactivation observed during operation may be related to the reducing reaction environment (absence of oxygen and presence of hydrogen), which could induce partial reduction of oxide components and the formation of excess oxygen vacancies.

To further contextualize these results, a comparison with representative $TiO_2$-based photocatalytic systems from the literature is provided in Table S3. Despite the use of a planar thin-film architecture, which inherently exhibits a lower surface-to-mass ratio than nanopowder or porous systems, the hydrogen production rates obtained in this work fall within the range of state-of-the-art $TiO_2$ photocatalysts. This comparison highlights that the performance achieved here is competitive with similar $TiO_2$/Au-based systems, while relying on a geometrical strategy for carrier management rather than optimization of catalyst composition or nanostructures.

### 3.3. Langmuir–Hinshelwood Geometric Kinetic Model

To understand the influence of the ETL geometry on our samples, it is first necessary to consider the reaction mechanism and kinetics. As in any heterogeneous catalytic system, the reactants must initially adsorb onto the surface. Adsorbed species can also desorb if the reaction does not proceed. In photocatalysis, desorption is possible because charge carriers are required to drive the redox reaction; without sufficient electrons or holes, the adsorbed molecules may desorb before reaction occurs. Once reactants are adsorbed and appropriate charge carriers are available, the reaction can proceed. While product desorption/readsorption can be important in some cases, it is negligible in our system because the reaction is performed in a continuous gas flow that constantly supplies fresh reactants and efficiently removes products. Under these conditions, desorption of products is rapid relative to the catalytic step. Based on these considerations, we can construct a reaction flow diagram for our system, where ethanol is the reactant and hydrogen and acetaldehyde are the products, as

described in Fig. 5a and eqn (1).

$$\overbrace{S + E \underset{k_-}{\overset{k_+}{\rightleftharpoons}} ES}^{\text{Adsorption}} \underbrace{\xrightarrow[2\cdot[e-h]]{k} H + A + S}_{\text{Ethanol dehydrogenation}} \quad (1)$$

In this scheme, $S$ denotes the active sites of the solid catalyst, $E$ is the ethanol concentration or partial pressure, and $ES$ represents active sites occupied by adsorbed ethanol. The term [e–h] refers to the concentration of photogenerated electron–hole pairs that reach the surface or the adsorbed reactants and are able to drive the photocatalytic reaction. $H$ and $A$ correspond to the concentrations or partial pressures of hydrogen and acetaldehyde, respectively. The kinetic constants $k_\pm$ and $k_-$ describe the adsorption and desorption rates of ethanol, while $k$ is the intrinsic rate constant of the ethanol dehydrogenation step. From this eqn (1), we can write the time derivative of each species involved in the reaction as follows:

$$\frac{dE}{dt} = +k_- \cdot ES - k_+ \cdot E \cdot S \quad (2)$$

$$\frac{dH}{dt} = \frac{dA}{dt} = k \cdot ES \cdot [e-h]^2 \quad (3)$$

$$\frac{dES}{dt} = -\frac{dS}{dt} = k_+ \cdot E \cdot S - \left(k_- + k \cdot [e-h]^2\right) ES \quad (4)$$

We assume that the active sites with adsorbed ethanol rapidly reach a steady-state concentration ($d[ES]/dt = 0$), since the adsorption process is much faster than the dehydrogenation reaction, which constitutes the rate-limiting step. We also define $S_0$ as the total fixed number of active sites on the catalyst ($S_0 = S + ES$, with $dS_0/dt = 0$). With these assumptions and definitions, we can proceed to formulate the kinetic expressions.

$$\frac{dES}{dt} = k_+ \cdot E \cdot (S_0 - ES) - \left(k_- + k \cdot [e-h]^2\right) ES = 0$$
$$\rightarrow ES = \frac{k_+ \cdot S_0 \cdot E}{k_- + k \cdot [e-h]^2 + k_+ \cdot E} \quad (5)$$

$$\frac{dH}{dt} = k \cdot ES \cdot [e-h]^2 = \frac{k_+ \cdot S_0 \cdot k \cdot E \cdot [e-h]^2}{k_- + k \cdot [e-h]^2 + k_+ \cdot E} \quad (6)$$

$$\frac{dH}{dt} = \frac{k_+ \cdot S_0 \cdot k \cdot E \cdot [e-h]^2}{k_- + k \cdot [e-h]^2 + k_+ \cdot E} = k_{app} \frac{K \cdot [e-h]^2}{1 + K \cdot [e-h]^2} \begin{cases} k_{app} = k_+ \cdot S_0 \\ K = \dfrac{k}{k_- + k_+ \cdot E} \end{cases} \quad (7)$$

As shown, this expression links the hydrogen production rate to both the ethanol concentration and the number of charge carriers available to catalyze the reaction. All photocatalytic experiments were carried out under dynamic conditions that guarantee a constant ethanol flow over the photocatalyst,

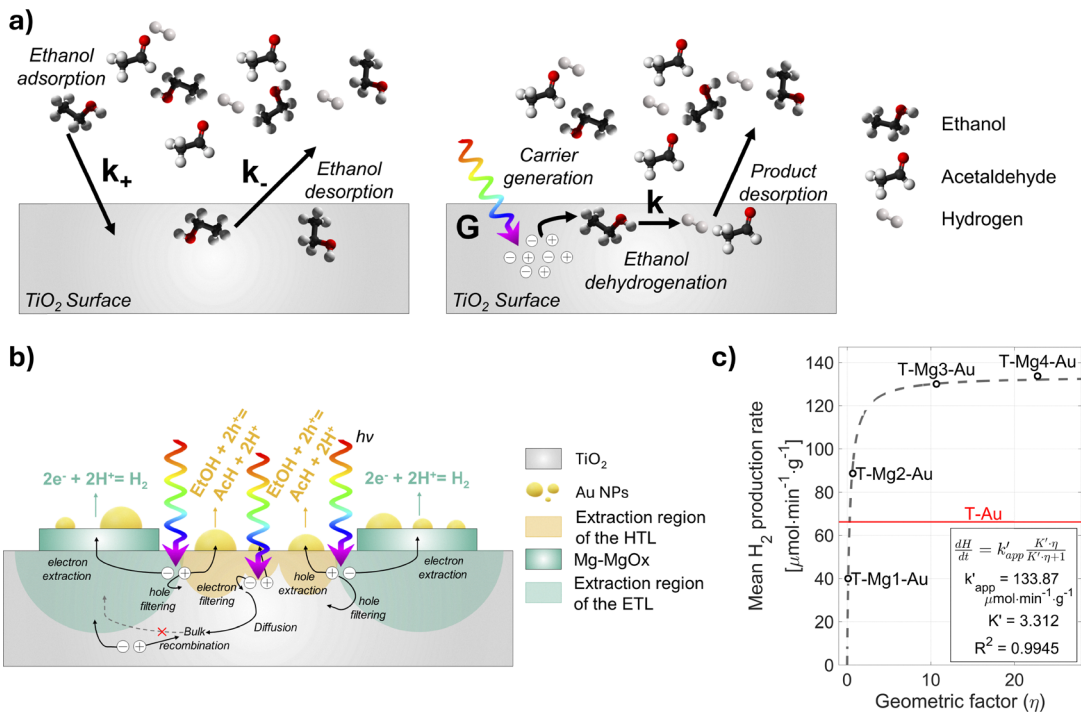


Fig. 5 (a) Schematic of the processes and reactions described by the Langmuir–Hinshelwood model for heterogeneous photocatalysis. (b) Electronic processes, charge filtering and carrier extraction in the interdigitated samples, with illustrative extraction regions associated with each selective contact. (c) Langmuir–Hinshelwood geometric kinetic model fitting of eqn (9) applied to the mean reaction rate of the interdigitated samples, compared to the T–Au($TiO_2$/Au) reference.

and this amount was identical across all measurements. Once the system reaches steady state, the ethanol concentration can therefore be treated as constant ($E$ = const → $dE/dt = 0$). In this form, the expression essentially reduces to a conventional Langmuir–Hinshelwood model,[40,41] but with the explicit inclusion of charge carriers as one of the reacting species under constant supply, while the other reactant remains at steady state.

In our experiment we defined a geometric factor, $\eta$, that captures the trends we observed between hydrogen production and the geometry of the Mg–$MgO_x$ pattern:

$$\eta = \left(\frac{\text{Perimeter ETL}}{\text{Substrate Perimeter}}\right) \Big/ \left(\frac{\text{Area ETL}}{\text{Substrate Area}}\right) \tag{8}$$

As shown in eqn (8), $\eta$ is obtained by normalizing the Mg–$MgO_x$ perimeter by the substrate perimeter and dividing this by the normalized Mg–$MgO_x$ area. In practice, the denominator corresponds to the fractional coverage. The result is a dimensionless parameter that highlights how much interfacial length is available per unit of covered area, which helps rationalize why samples with comparable coverage may nonetheless exhibit markedly different photocatalytic behavior. The physical meaning of this parameter can be interpreted as the ratio between the effective extraction interface, represented by the Mg–$MgO_x$ perimeter, and the corresponding extraction area, *i.e.*, the Mg–$MgO_x$ coverage. Both quantities are normalized by the substrate perimeter and area, respectively, to account for small variations between samples and to ensure that $\eta$ remains a dimensionless descriptor.

If we plot the mean hydrogen production rate of each sample against the geometric factor $\eta$ (Fig. 5c), we observe that the data follow eqn (9) with remarkable accuracy:

$$\left(\frac{dH}{dt}\right)_{\text{mean}} = k'_{\text{app}} \frac{K' \cdot \eta}{1 + K' \cdot \eta} \begin{cases} k'_{\text{app}} = 133.87\ \mu\text{mol min}^{-1}\ \text{g}^{-1} \\ K' = 3.312 \end{cases} \tag{9}$$

Eqn (9) has the same functional form as eqn (7), except that the rate is expressed as a function of the geometric parameter rather than the square charge-carrier concentration. Because the surface composition of all samples is identical, we can assume that intrinsic adsorption and desorption rates ($k_+$ and $k_-$) and the fundamental dehydrogenation rate ($k$) are the same. The samples also have comparable dimensions, and all rates have been normalized to the amount of photocatalytically active $TiO_2$. Consequently, the total number of active sites $S_0$ can be considered similar across the series.

Under these conditions, the parallel behavior of both expressions suggests that optimizing the ETL pattern effectively increases the number of charge carriers that reach catalytic sites and participate in the reaction. In other words, the geometric design controls how efficiently carriers avoid recombination and are extracted through the selective contacts. Patterns with a larger perimeter provide more interface length through which carriers can be collected, a feature that becomes crucial when the carrier diffusion length (or, equivalently, lifetime) is relatively short. To minimize recombination losses, carriers generated anywhere in the absorber must quickly enter the influence region of either the hole- or electron-selective contact (Fig. 5b). This influence region corresponds to the size of the space charge region formed at the ETL-absorber and HTL-absorber junctions.

It is important to note that this Langmuir–Hinshelwood geometric–kinetic framework is primarily applicable to planar architectures, where both area and perimeter can be unambiguously defined, as in the present case. The model further relies on the assumption of sufficiently selective transport layers and on a characteristic carrier diffusion length that is comparable to or smaller than the spacing between extraction regions. Under these conditions, carrier collection is limited by the distance to the nearest selective interface, and the perimeter density becomes a meaningful descriptor of extraction efficiency. In contrast, if the diffusion length is sufficiently large, photogenerated carriers can readily reach both selective contacts regardless of their spatial arrangement, reducing the dependence on interdigitation. In the present system, this condition is satisfied: the Mg–$MgO_x$ layer defines discrete electron-selective domains, while the Au nanoparticles form a spatially distributed hole-selective network, making the geometry of the electron-selective interface the dominant factor governing carrier extraction.

Within this framework, an effective ETL pattern is one that maximizes perimeter while using only the necessary fraction of active area to enhance electron extraction. This balance ensures that the system benefits simultaneously from rapid majority-carrier extraction and sufficient uncovered $TiO_2$ surface for minority-carrier transfer, which together determines the overall photocatalytic performance.

# 4. Conclusions

Interdigitated front selective contacts based on Mg–$MgO_x$ and Au have been fabricated and tested for photocatalytic hydrogen generation from ethanol-containing gas mixtures. The results show that the geometry of the ETL plays a decisive role in determining the photocatalytic efficiency of the system. The combination of Mg–$MgO_x$ as the electron-selective layer and Au as both hole extractor and plasmonic activator reaches its full potential only when both materials are arranged in patterns that balance extraction and recombination. Simply increasing the Mg–$MgO_x$ coverage cannot account for the differences observed among samples. The geometric parameter $\eta$, which relates perimeter to coverage, provides a quantitative way to describe this effect: as $\eta$ increases, the available interface length for carrier collection expands, and the reaction shifts into a more efficient regime, seen in higher initial rates and greater hydrogen output. Stability tests further show that the optimized interdigitated architectures maintain a significant fraction of their activity over extended operation times, confirming that the performance gains are not limited to short-term measurements.

Fitting the Langmuir–Hinshelwood model using $\eta$ as the active variable reproduces the experimental behavior with high accuracy. This suggests that the ETL architecture effectively modulates the carrier density reaching the adsorbed reactants. The most interdigitated samples, especially T–Mg3–Au and T–Mg4–Au, show a substantial increase in activity that cannot be explained by the amount of Mg–$MgO_x$ or the number of Au nanoparticles. Instead, the improvement arises from the creation of densely spaced extraction regions that shorten diffusion distances and suppress recombination.

Overall, the work demonstrates that the geometric design of selective contacts is as crucial as the composition of the photocatalyst itself. These results also highlight that, for practical implementation, the long-term stability of the transport layers within the interdigitated architecture is essential to sustain efficient hydrogen production. Interdigitated architectures offer a direct and scalable route to optimize oxide-based systems with metallic nanoparticles, and the framework developed here can be extended to other photo-driven reactions where spatial management of carriers limits efficiency. The geometric engineering strategy outlined in this study provides a simple method to tune surface kinetics through controlled charge extraction, enabling improved performance without altering the chemistry of the active absorber. Looking ahead, a flatter absorber would open the door to advanced lithography or precision stencil deposition, allowing tighter control over the ETL perimeter and the incorporation of an interdigitated HTL layer. Such HTLs could rely on high-work-function oxides which, thanks to their wide bandgap, remain transparent while acting as effective hole-selective contacts.[42] On top of this layered architecture, Au nanoparticles could be integrated to enhance plasmonic generation and facilitate charge transfer from the solid-state catalyst toward the gas phase and the reacting species, giving the system another lever to boost activity.

These results demonstrate that the geometry of selective contacts is as important as their chemical composition in photocatalysis. By engineering interdigitated electron- and hole-selective regions, carrier diffusion distances are shortened, recombination is suppressed, and surface reaction rates are enhanced without modifying the absorber chemistry. This geometric strategy provides a scalable route to optimize oxide-based photocatalysts and can be extended to other photo-driven reactions where spatial management of charge carriers limits performance.

## Author contributions

O.S.B. was responsible for the conceptualization, sample fabrication, data acquisition, formal analysis and wrote the original draft. E.M., E.R. and A.A. help with sample fabrication, data acquisition and formal analysis. L.C.B. performed the XPS measurements and analysis. J.L., L.S., E.S., M.P., C.V. and J.P.G. supervised E.M., A.A., E.R. and O.S.B., did conceptualization and contributed to funding acquisition. All authors contributed to discussions and to writing, review & editing.

## Conflicts of interest

There are no conflicts to declare.

## Data availability

The processed datasets supporting the findings of this study, including time-resolved H2 and acetaldehyde production rates and illumination periods for all samples, are publicly available and will be deposited on Zenodo (https://zenodo.org/records/19347867?token=eyJhbGciOiJIUzUxMiJ9.eyJpZCI6IjEyZGE4OTA0LTM3NDgtNDI1Mi05NGYzLThhZTA0MTJlOGNlOSIsImRhdGEiOnt9LCJyYW5kb20iOiJjM2RhMzAyNThlMjJkMDEyNzYwOGVjMjVmMjBkOTNiMSJ9.5wKARrQgUAk6EZkIk0OE8_12wbRxxtvLkiX99OBDi4wmvoqQ25fvAXDRCggvVNs5_RQjqz_TRAMKGdEB8tu7jA). These datasets are accompanied by a README file describing sample types and data structure, enabling verification and reuse of the results. The raw experimental data are not currently publicly available due to their large size and contextual metadata requirements but can be obtained from the corresponding author upon reasonable request.

Supplementary information (SI): the supplementary information compiles the experimental and structural data supporting the main conclusions of the study. It includes the full detailed Experimental section, providing complete descriptions of sample fabrication, characterization, and photocatalytic measurements. It also includes the emission spectrum of the solar simulator used during photocatalytic measurements, along with Raman spectra confirming the anatase phase of the sol–gel $TiO_2$ absorber. A complete set of 3D schematic models describes the architecture of each sample, including sample codes, pattern geometry, and the defining ETL parameters. Additional SEM images at different magnifications illustrate the surface morphology of both the bare $TiO_2$ layer and the Mg–$MgO_x$/Au-modified films. Complementary XPS measurements of Ti 2p and O 1s core levels for selected samples further validate the chemical composition and oxidation behavior discussed in the main text. The supplementary section also presents the hydrogen and acetaldehyde production profiles for all samples, together with a detailed table listing the geometric characteristics of the ETL patterns and the key photocatalytic metrics extracted from the first two hours of reaction. See DOI: https://doi.org/10.1039/d6ey00024j.

## Acknowledgements

This project received funding from the European Union's H2020 ERC-Consolidator programme under grant agreement number no. 866018 (SENSATE), and by the Science and Innovation Ministry of Spain projects number PID2023-148976OB-C41/C44 (CURIO-CITY) and PCI2023-145971-2 (ACT-FAST, CET-Partnership 2023 program), PID2022-140226OB-C31C32

(INNO-PV), PID2022-138434OB-C51 (SCALING), MICIN/FEDER PID2024-156765OB-C21, PCI2024-155100-2 (ENPOWER, CETP-Partnership Program 2023), funded by MCIN/AEI/10.13039/501100011033/FEDER, and CNS2023-14817 (SELECTRON) funded by MCIN/AEI/10.13039/501100011033/NextGenerationEU/PRTR. Some of the authors from UPC belong to the Micro and Nanotechnologies for Solar Energy Group (MNT-Solar) Consolidated Research Group of the ''Generalitat de Catalunya'' (2021 SGR 01286). This work is also part of Maria de Maeztu Units of Excellence Programme CEX2023-001300-M/ funded by MICIU/AEI/10.13039/501100011033. O.S.B. is grateful to the Science and Innovation Ministry of Spain for the FPI fellowship no. PREP2023-001768. E.S. is grateful to ICREA Academia program. J.L is a Serra Húnter Fellow and is grateful to the Academia Excellence program (Generalitat de Catalunya). E.R. acknowledges support from 'Departament de Recerca i Universitats: del Departament d'Acció Climàtica, Alimentació i Agenda Rural i Fons Climàtic de la Generalitat de Catalunya' with the grant 2023CLIMA00022.

## References

1 F. Xu and B. Weng, Photocatalytic hydrogen production: an overview of new advances in structural tuning strategies, *J. Mater. Chem. A*, 2023, **11**(9), 4473–4486.

2 S. O. Akpasi, I. M. Smarte Anekwe, E. K. Tetteh, U. O. Amune, S. I. Mustapha and S. L. Kiambi, Hydrogen as a clean energy carrier: advancements, challenges, and its role in a sustainable energy future, *Clean Energy*, 2025, **9**(1), 52–58.

3 Y. Chen, A. Agrelo-Lestón, I. Burgués-Ceballos, J. Llorca and L. Soler, Bimetallic Nanoparticles as Cocatalysts for Photocatalytic Hydrogen Production, *Adv. Funct. Mater.*, 2025, **36**(21), e06279.

4 S. Ghasemi, A. Parastesh, M. Padervand, H. Ren, X. Li, A. Labidi, M. Signoretto, E. A. Dawi, T. Hamzehlouyan, E. Lichtfouse and C. Wang, Recent progress on Z- and S-scheme photocatalysis: mechanistic understanding toward green applications, *Curr. Opin. Chem. Eng.*, 2025, **47**, 101059.

5 Y. Yuan, J. Pan, W. Yin, H. Yu, F. Wang, W. Hu, L. Wang and D. Yan, Effective strategies to promote Z(S)-scheme photocatalytic water splitting, *Chin. Chem. Lett.*, 2024, **35**(3), DOI: 10.1016/j.cclet.2023.108724.

6 J. Puigdollers, C. Voz and E. Ros, Physics and Technology of Carrier Selective Contact Based Heterojunction Silicon Solar Cells, in *Energy Harvesting and Storage*, 2022, pp. 61–95.

7 M. R. Nellist, F. A. L. Laskowski, F. Lin, T. J. Mills and S. W. Boettcher, Semiconductor-Electrocatalyst Interfaces: Theory, Experiment, and Applications in Photoelectrochemical Water Splitting, *Acc. Chem. Res.*, 2016, **49**, 733–740.

8 M. Schleuning, I. Y. Ahmet, R. van de Krol and M. M. May, The role of selective contacts and built-in field for charge separation and transport in photoelectrochemical devices, *Sustainable Energy and Fuels*, 2022, **6**(16), 3701–3716.

9 M. A. Green, E. D. Dunlop, M. Yoshita, N. Kopidakis, K. Bothe, G. Siefer, X. Hao and J. Y. Jiang, Solar Cell Efficiency Tables (Version 66), *Prog. Photovoltaics Res. Appl.*, 2025, **33**, 795–810.

10 O. Almora, A. O. Alvarez, D. Baran, C. I. Cabrera, L. A. Castriotta, B. Ehrler, S. Erten-Ela, K. Fukuda, F. Guo, J. Hauch, A. W. Y. Ho-Baillie, T. J. Jacobsson, R. A. J. Janssen, T. Kirchartz, M. A. Loi, R. R. Lunt, X. Mathew, J. Min, D. B. Mitzi, M. K. Nazeeruddin, A. F. Nogueira, U. W. Paetzold, N. Park, B. P. Rand, H. Snaith, T. Someya, C. Sprau, L. Sun, K. Forberich and C. J. Brabec, Device Performance of Emerging Photovoltaic Materials (Version 6), *Adv. Energy Mater.*, 2025, **16**(7), e05525.

11 C. Ballif, F. J. Haug, M. Boccard, P. J. Verlinden and G. Hahn, Status and perspectives of crystalline silicon photovoltaics in research and industry, *Nat. Rev. Mater.*, 2022, **7**, 597–616.

12 K. Khan, X. Tao, Y. Zhao, B. Zeng, M. Shi, N. Ta, J. Li, X. Jin, R. Li and C. Li, Spatial separation of dual-cocatalysts on one-dimensional semiconductors for photocatalytic hydrogen production, *J. Mater. Chem. A*, 2019, **7**, 15607–15614.

13 S. Zhu, W. Liao, M. Zhang and S. Liang, Design of spatially separated Au and CoO dual cocatalysts on hollow $TiO_2$ for enhanced photocatalytic activity towards the reduction of $CO_2$ to $CH_4$, *Chem. Eng. J.*, 2019, **361**, 461–469.

14 X. Jin, R. Li, Y. Zhao, X. Liu, X. Wang, H. Jiao and J. Li, Spatial separation of dual-cocatalysts on bismuth vanadate for selective aerobic oxidation of benzylalcohols to benzaldehydes under visible light irradiation, *Catal. Sci. Technol.*, 2018, **8**, 6173–6179.

15 W. Li, Z. Xu, Y. Yan, J. Zhou, Q. Huang, S. Xu, X. Zhang, Y. Zhao and G. Hou, Passivating Contacts for Crystalline Silicon Solar Cells: An Overview of the Current Advances and Future Perspectives, *Adv. Energy Mater.*, 2024, **14**(18), 2304338.

16 W. Ahmad, C. Li, W. Yu and P. Gao, Revolutionizing photovoltaics: From back-contact silicon to back-contact perovskite solar cells, *Mater. Today Electron.*, 2024, **9**, 100106.

17 P. She, H. Rao, B. Guan, J. S. Qin and J. Yu, Spatially Separated Bifunctional Cocatalysts Decorated on Hollow-Structured $TiO_2$ for Enhanced Photocatalytic Hydrogen Generation, *ACS Appl. Mater. Interfaces*, 2020, **12**, 23356–23362.

18 S. Wang, G. Liu and L. Wang, Crystal Facet Engineering of Photoelectrodes for Photoelectrochemical Water Splitting, *Chem. Rev.*, 2019, **119**(8), 5192–5247.

19 Y. Zhang, X. Wu, Z. H. Wang, Y. Peng, Y. Liu, S. Yang, C. Sun, X. Xu, X. Zhang, J. Kang, S. H. Wei, P. F. Liu, S. Dai and H. G. Yang, Crystal Facet Engineering on $SrTiO_3$ Enhances Photocatalytic Overall Water Splitting, *J. Am. Chem. Soc.*, 2024, **146**(10), 6618–6627.

20 Q. Shen, W. Kang, L. Ma, Z. Sun, B. Jin, H. Li, Y. Miao, H. Jia and J. Xue, Tuning the anisotropic facet of $SrTiO_3$ to promote spatial charge separation for enhancing photocatalytic $CO_2$ reduction properties, *Chem. Eng. J.*, 2023, **478**, 147338.

21 J. Zhang, P. Zhou, J. Liu and J. Yu, New understanding of the difference of photocatalytic activity among anatase, rutile and brookite $TiO_2$, *Phys. Chem. Chem. Phys.*, 2014, **16**, 20382–20386.
22 J. L. K. Gbe, K. Ravi, M. Singh, S. Neogi, M. Grafouté and A. V. Biradar, Hierarchical porous nitrogen-doped carbon supported MgO as an excellent composite for $CO_2$ capture at atmospheric pressure and conversion to value-added products, *J. CO2 Util.*, 2022, **65**, 102222.
23 Y. J. Heo and S. J. Park, Facile Synthesis of MgO-Modified Carbon Adsorbents with Microwave-Assisted Methods: Effect of MgO Particles and Porosities on $CO_2$ Capture, *Sci. Rep.*, 2017, **7**(1), 5653.
24 Y. Wan, C. Samundsett, J. Bullock, M. Hettick, T. Allen, D. Yan, J. Peng, Y. Wu, J. Cui, A. Javey and A. Cuevas, Conductive and Stable Magnesium Oxide Electron-Selective Contacts for Efficient Silicon Solar Cells, *Adv. Energy Mater.*, 2017, **7**(5), 1601863.
25 A. N. Cho and N. G. Park, Impact of Interfacial Layers in Perovskite Solar Cells, *ChemSusChem*, 2017, **10**(19), 3687–3704.
26 X. Guo, H. Dong, W. Li, N. Li and L. Wang, Multifunctional MgO layer in perovskite solar cells, *Chem. Phys. Chem.*, 2015, **16**, 1727–1732.
27 I. A. Mkhalid, Visible light photocatalytic synthesis of aniline with an Au/$LaTiO_3$ nanocomposites, *J. Alloys Compd.*, 2015, **631**, 298–302.
28 M. K. Aulakh and B. Pal, Influence of co-catalyst amount/size for selective hydrogenation of 1,3-dinitrobenzene over Au-m$TiO_2$ nanocomposites under visible light, *Adv. Powder Technol.*, 2019, **30**, 1329–1337.
29 M. A. Brown, Y. Fujimori, F. Ringleb, X. Shao, F. Stavale, N. Nilius, M. Sterrer and H. J. Freund, Oxidation of Au by surface OH: Nucleation and electronic structure of gold on hydroxylated MgO(001), *J. Am. Chem. Soc.*, 2011, **133**, 10668–10676.
30 G. N. Derry, M. E. Kern and E. H. Worth, Recommended values of clean metal surface work functions, *J. Vac. Sci. Technol., A*, 2015, **33**(6), 060801.
31 S. Kashiwaya, J. Morasch, V. Streibel, T. Toupance, W. Jaegermann and A. Klein, The Work Function of $TiO_2$, *Surfaces*, 2018, **1**, 73–89.
32 T. Zhao, D. Solanki, Z. Pan and S. Hu, Charge Separation in Photocatalysts: Mechanisms, Physical Parameters, and Design Principles, *ACS Energy Lett.*, 2023, **7**(1), 432–452.
33 Y. Chen, L. Soler, M. Armengol-Profitós, C. Xie, D. Crespo and J. Llorca, Enhanced photoproduction of hydrogen on Pd/$TiO_2$ prepared by mechanochemistry, *Appl. Catal., B*, 2022, **309**, 121275.
34 S. T. Kochuveedu, Y. H. Jang and D. H. Kim, A study on the mechanism for the interaction of light with noble metal-metal oxide semiconductor nanostructures for various photophysical applications, *Chem. Soc. Rev.*, 2013, **42**, 8467–8493.
35 A. Castedo, A. Casanovas, I. Angurell, L. Soler and J. Llorca, Effect of temperature on the gas-phase photocatalytic $H_2$ generation using microreactors under UVA and sunlight irradiation, *Fuel*, 2018, **222**, 327–333.
36 N. Chaulagain, K. M. Alam, S. Kadian, N. Kumar, J. Garcia, G. Manik and K. Shankar, Synergistic Enhancement of the Photoelectrochemical Performance of $TiO_2$ Nanorod Arrays through Embedded Plasmon and Surface Carbon Nitride Co-sensitization, *ACS Appl. Mater. Interfaces*, 2022, **14**, 24309–24320.
37 O. Henrotte, Š. Kment and A. Naldoni, Interfacial States in Au/Reduced $TiO_2$ Plasmonic Photocatalysts Quench Hot-Carrier Photoactivity, *J. Phys. Chem. C*, 2023, **127**, 15861–15870.
38 S. Pandey, S. Joseph, S. Majumdar, J. Ahuja, S. Devinder, S. A. Siddiqui, K. Ghosh and J. Joseph, Engineering plasmonic charge kinetics and broadband photoelectrochemical spectral responses using a multi-resonant Au-$TiO_2$ plasmonic particle grating-based optical resonator, *Nanoscale*, 2024, **17**, 1105–1118.
39 C. Ding, J. Shi, Z. Wang and C. Li, Photoelectrocatalytic Water Splitting: Significance of Cocatalysts, Electrolyte, and Interfaces, *ACS Catal.*, 2017, **7**, 675–688.
40 D. F. Ollis, Kinetics of Photocatalyzed Reactions: Five Lessons Learned, *Front. Chem.*, 2018, **6**, 378.
41 H. D. Tran, D. Q. Nguyen, P. T. Do and U. N. P. Tran, Kinetics of photocatalytic degradation of organic compounds: a mini-review and new approach, *RSC Adv.*, 2023, **13**, 16915–16925.
42 O. Segura-Blanch, A. Torrens, A. Jimenez-Arguijo, L. Garcia-Carreras, L. Calvo-Barrio, J. M. Asensi, J. Puigdollers, M. Placidi and E. Saucedo, Understanding the Role of Transition Metal Oxides as Hole-Selective Contacts for Enhanced Efficiency in Selenium Solar Cells, *ACS Appl. Energy Mater.*, 2025, **8**(22), 16729–16738.